

Design and Characterization of a Robotic Cyber-Physical System for Real-Time Flow-Device Experiments*

Emile Moreau¹, Benoît Herman¹, Philippe Chatelain¹ and Renaud Ronsse¹

Abstract—This paper presents the design and the experimental characterization of a Cyber-Physical System tailored for research in fundamental and applied fluid mechanics (fluid-structure interaction problems), biomechanics (biolocomotion), and civil engineering (wind- or flow-structure interactions). The design is aimed at ideally controlling the six degrees of freedom of the manipulated object, being versatile to different experimental scenarios, and usable in real-time and closed-loop if manipulating an active object. Mechanical design robustness is examined through an experiment emphasizing the crucial constraint of robot rigidity. Subsequently, the robotic Cyber-Physical System kinematic and dynamic capabilities are validated, demonstrating compliance to specifications, along with considerations regarding acceleration saturation. A third experiment analyzes the robot end-effector natural frequencies, yielding frequency ranges that should not be excited in future experiments. Findings contribute to providing directions for refining the mechanical design, synthesizing control strategies, and enhancing the device robustness and performance in various flow-device interaction scenarios.

I. INTRODUCTION

A wake is the signature of a device moving in a flow producing forces or extracting energy from this medium [1]. These flow structures can then impact negatively or favorably another device downstream. Wake turbulence between aircraft in air traffic [2, 3] and energy exchange between water and eel-like robot are prime examples of this phenomenon [4]–[7]. Migrating birds adopting a V-shaped flight formation can exploit vortices shed by the individuals upfront in order to decrease their energetic cost, at least if they coordinate their gait in an appropriate way [8, 9]. This efficient exploitation of wakes is not straightforward however: wakes are complex and turbulent flows. The stabilization of a device or an animal in a turbulent wake requires robust flow sensing and control strategies. These observations have led to many research efforts on controller synthesis, yet using simplified models of the turbulent flow [10]. These models thus give a limited representation of the flow and the resulting developments lack adaptivity and robustness when faced with the reality gap. It is thus essential to complement these numerical investigations with real experiments governed by the same physics as the original system.

A large amount of aero- and hydro-dynamics experiments entail a scaled device held in place by means of a minimally disruptive manipulator, such as Captive Trajectory Systems, which naturally affects the dynamics of a freely-flying or

swimming device [11]. Indeed, this impacts the reproduction of realistic kinematics or dynamics for the device, while the holding arm will also transfer momentum to the device. This spurious momentum flux will manifest itself in the flow structures (the wake) shed by the device. These systems have been used in the past, but mostly for specific scenarios in aerospace engineering. Applications of such systems to biolocomotion and formation flight are extremely scarce, **because of their non real-time behavior**. Cyber-Physical Systems (CPS) address this gap: they are integrated systems combining the advantages of physical experimentation with the flexibility and intelligence of digital systems [12, 13]. This integration allows researchers to study and manipulate flow behavior in real-time, gather data, and control experimental setups efficiently, enabling cutting-edge research and advancements in fluid dynamics. By incorporating CPS in their investigations, researchers can optimize experimental parameters and conditions more efficiently. Automated systems can explore a broader range of parameters and configurations, leading to quicker identification of optimal setups and experimental designs [14]. **Such systems have been used for fluid-structure interaction experiments with a foil, a cylinder, a plate, or a flexible wing [15]–[19]. These experiments typically involved one or two Degrees-of-Freedom (DoFs) motions in a wind tunnel or a water tunnel.**

With the long-term objective of performing real-time flow-device interaction experiments with six DoFs, i.e. three translations along the Cartesian axes and three rotations about these axes, this paper reports the design of an innovative robotic CPS. This system not only enables the actuation of six DoFs but also facilitates experiments in either a wind tunnel or a water towing tank. The primary objective of this robotic system is to regulate the motions of a physical device

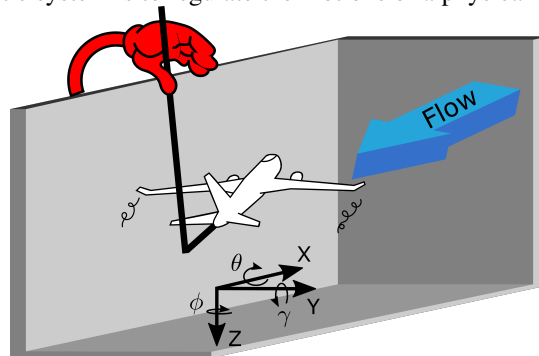


Fig. 1. Six DoFs CPS for real-time flow-device interactions experiments. The layout shows a plane i.e. a typical object to be manipulated, and a virtual hand manipulating the plane, which idealizes the target design of the CPS.

¹ Institute of Mechanics, Materials, and Civil Engineering, UCLouvain, 1348 Louvain-la-Neuve, Belgium emile.moreau@uclouvain.be

* This work was supported by the Fonds de la Recherche Scientifique - FNRS under Grant n° 33678993

using a combination of (zero) force, impedance, and/or position control. The device will then fly/swim/fall freely in the fluid and the robot will be able to render virtual impedances (mass and/or damping and/or stiffness and/or gravity), to impose pre-determined force profiles (e.g. thrust), and to precisely measure its displacements. A schematic description of the setup in a typical experimental configuration, i.e. a cyber-physical system performing the experiment of a plane freely flying in a flow, is illustrated in Figure 1.

This paper first presents the current robot design with a reduced number of DoFs. Then it elaborates on the experimental methodology employed to conduct its thorough characterization. The paper ends with the experimental perspectives offered by this new and unique CPS.

II. ROBOT OVERVIEW

A. Main Specifications

To enable six DoFs real-time dynamic experiments exploring flow-device interaction, the CPS has been designed to cater three representative scenarios, encompassing considerations such as workspace, **accuracy**, dynamics, and rigidity. The first scenario consists in handling a cylinder submerged in a fluid, inducing transverse oscillations with at least two DoFs (Y translation and ϕ rotation, see Figure 1 for frame definition) [12]. The second scenario involves a eel-like swimming robot, with the CPS regulating the three DoFs in the transverse plane (X and Y translations axis and ϕ rotation) in force/torque or admittance, such that the robot can move only in the transverse plane. The third scenario, captured in Figure 1, entails a freely flying plane, necessitating the management of all six DoFs in admittance. The experimental scenarios encompass a broad spectrum, spanning from air, with fluid flow velocities reaching up to 15 m s^{-1} , to water, with fluid flow relative velocities reaching up to 1 m s^{-1} . These experiments also involve varying degrees of complexity, with Reynolds numbers extending up to 50000, demanding a versatile and robust CPS, placed above a towing tank or in a wind tunnel. The maximum velocity and acceleration specifications associated to each experiment are presented in Table I. Gathering all these design constraints, we came to the following specifications. The workspace should be a 0.6 m cube. Dynamic specifications include

TABLE I
MAXIMUM VELOCITY AND ACCELERATION SPECIFICATIONS
ASSOCIATED TO EACH EXPERIMENTAL SCENARIO AND FOR EACH
CARTESIAN DIRECTION.

Cartesian direction	Velocity [m s^{-1}]			Acceleration [m s^{-2}]		
	X	Y	Z	X	Y	Z
Cylinder	/	0.2	/	/	0.2	/
Eel	0.2	0.1	/	0.1	0.5	/
Plane	1	2	1	2	7	2

maximum velocities and accelerations for each Cartesian axis, defined as $\dot{X}_{max} = \dot{Z}_{max} = 1 \text{ m s}^{-1}$, $\dot{Y}_{max} = 2 \text{ m s}^{-1}$, $\ddot{X}_{max} = \ddot{Z}_{max} = 2 \text{ m s}^{-2}$ and $\ddot{Y}_{max} = 7 \text{ m s}^{-2}$. **Accuracy** requirements dictate that the robot end-effector maintains a position error within 1 mm and an angular error of 0.1° . These specifications collectively define the CPS operational parameters, ensuring its efficacy in target experimental scenarios.

To date and in the rest of this paper, the designed robot implementing the CPS is composed of the four first DoFs, i.e. the three translations and the ϕ rotation.

B. Electromechanical Design

The outcome of the robot mechanical design is illustrated in Figure 2. The colored cubes denote the CPS workspace: in green, the terminal one, i.e. once the robot will be equipped with the last two DOFs, and in red, the proximal one, considered in the present study. The space left between these cubes will thus accommodate the electromechanical structure implementing the last two DOFs, i.e. rotations in θ and γ . Figure 2 highlights two main parts: the CPS and the mechanical structure supporting it. This structure has been meticulously designed for displaying high stiffness and is firmly anchored into the ground. The first three DoFs of the CPS are arranged according to a Cartesian robot configuration, and a fourth rotational DoF is added around the vertical axis of the Cartesian robot. The structural parts are made with *EN AW 6063-T66* aluminium profiles, with a Young's modulus of 70 GPa , provided by Vansichen n.v. (Hasselt, Belgium) and use belt transmissions. The robot contains a dual actuated transmission and guiding system

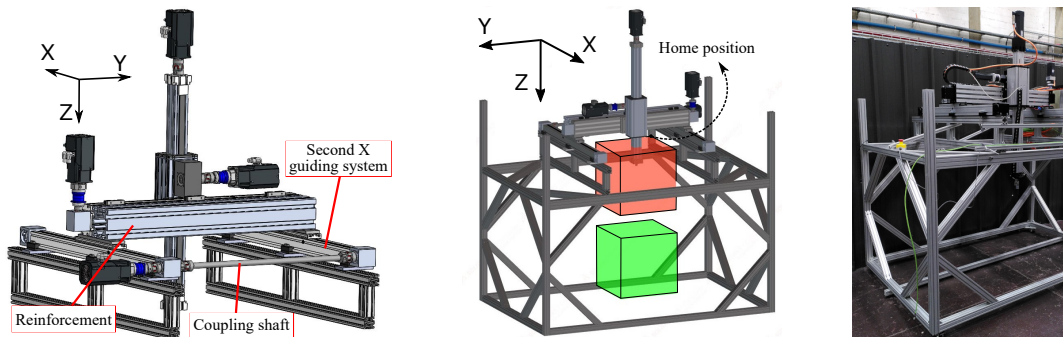


Fig. 2. Left: CAD drawing back view of the robotic CPS. Specific elements can be observed such as two X linear systems with the associated coupling shaft and reinforcement to increase system rigidity. Center: CAD drawing showing the four DoFs Cartesian robot, the supporting structure and the robot workspaces in green and red. The green workspace is the **terminal** workspace, when the system will be composed of six DoFs. The red one is the **proximal** one. Right: picture of the actual CPS, highlighting the four DoFs Cartesian robot and the supporting structure.

(denoted as a linear system hereafter) in the X direction. Power generated by the single motor is transmitted from the first linear system to the second one through a coupling shaft. The linear system along the Y direction is reinforced with a 160 mm square aluminium profile. The actuation of each linear system is described in Table II. All the motors and gearboxes are provided by Beckhoff (Verl, Germany).

The CPS holds four sensors, i.e. the motor encoders. These absolute encoders are used to measure the end-effector position and have a sensitivity of 3.36×10^{-5} , 2.1×10^{-5} and 2.44×10^{-5} mm for axes X, Y and Z respectively and 3.43×10^{-4} degree for axis ϕ . A 6 DoFs force/torque sensor is mounted at the extremity of the end-effector and has a measurement range of 250, 250 and 1000 N and 6, 6 and 3.4 N m for its X, Y and Z axes, respectively. This sensor is provided by ATI industrial automation (Apex, USA).

The robot controller consists of a double-cascaded PI controller (speed and current) in which gains have been tuned following the procedure recommended by the motors manufacturer [20].

The rest of this paper focuses on the characterization of the the first three DOFs (in translation), since these are the most affected by rigidity issues and inertial efforts.

III. EXPERIMENT 1 : RIGIDITY CHARACTERIZATION

A. Methods

The objective of the first experiment is to quantify the robot deformation under a static load applied to its end-effector and to determine the corresponding compliance matrix (C) describing the robot flexibility. The set-up is depicted in Figure 3. It comprises three dynamometers to gauge applied forces along each of the main axes, slender metal cables, three automatic lashing strap systems, and a *Polytec* (Baden-Württemberg, Germany) laser vibrometer offering precise measurements of small displacements. This sensor has a measurement range of 4 mm and a resolution of 2.38×10^{-7} mm, with an experimental **repeatability** evaluated at 6.5×10^{-2} mm. The robot joints are restricted by mechanical stop elements. Consequently, the deformation within the transmission chain is not taken into account. The robot position is chosen such that the deformation is maximal regarding a given level of external forces. This position is at the center of the workspace along axes X and Y and with full deployment along axis Z (lowest position).

The experiment proceeds with the following actions. Once the laser vibrometer is placed along one of the Cartesian axes (Y axis in Figure 3), the rest position is recorded. Then, the lashing strap are operated to set the desired forces

in the desired directions. Static forces measured with the dynamometers and the displacement measured with the laser vibrometer are recorded. These operations are reiterated until all the intended loads are captured along each of the Cartesian axes.

For each axis, four distinct loads are selected, evenly distributed across the specified range from the different scenarios, resulting in a total of 64 different external loads. By applying these loads and simultaneously recording the deflections along the three Cartesian axes, a total of 192 measurement points are recorded. As first order model, the following equation is used to determine the compliance matrix C of the robot, i.e. the linear relationship between applied forces $(F_x, F_y, F_z)^T$ and resulting deformations $(\Delta_x, \Delta_y, \Delta_z)^T$:

$$\begin{pmatrix} \Delta_x \\ \Delta_y \\ \Delta_z \end{pmatrix} = \begin{pmatrix} c_{11} & c_{12} & c_{13} \\ c_{21} & c_{22} & c_{23} \\ c_{31} & c_{32} & c_{33} \end{pmatrix} \begin{pmatrix} F_x \\ F_y \\ F_z \end{pmatrix} \quad (1)$$

The terms of the compliance matrix $c_{i,j}$ can then be estimated to the least-square sense by using the series of 192 trials corresponding to different applied forces and resulting displacements.

During these experiments, the robot is operated without any external load. This means that there is no fluid flow, and no object attached to the end-effector.

B. Results

The results of the first experiment offer insights into the end-effector rigidity across the three Cartesian directions relative to the applied forces. Equation 2 reports the compliance matrix in mm N^{-1} computed from experimental data:

$$C = \begin{pmatrix} 1.1 \cdot 10^{-2} & -2.83 \cdot 10^{-4} & -5.44 \cdot 10^{-4} \\ -1.73 \cdot 10^{-4} & 4.97 \cdot 10^{-3} & -4.68 \cdot 10^{-4} \\ -2.28 \cdot 10^{-3} & 8.29 \cdot 10^{-4} & 4.15 \cdot 10^{-4} \end{pmatrix} \quad (2)$$

In Figure 4, the displacement of the end-effector is show-cased for each direction, highlighting the effects of different forces exclusively applied in the corresponding direction. The dashed line represents the maximal deflection according to the specifications.

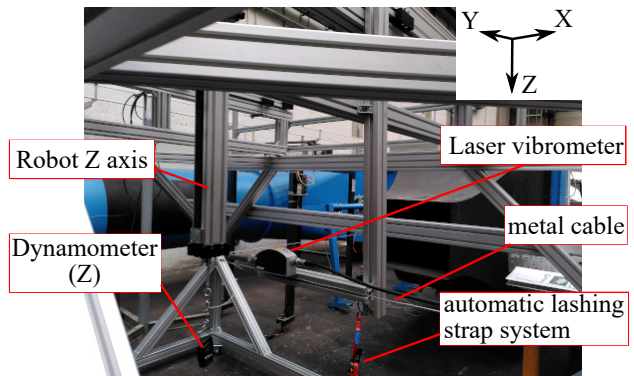


Fig. 3. External loads are induced by tensioning a metal cable through a lashing strap system. This loading force is precisely measured by a dynamometer, and the resulting end-effector deflection is measured by a laser vibrometer.

TABLE II

DESCRIPTION OF THE ACTUATION SYSTEMS OF THE ROBOT.

Linear system	Motor name	Nominal rotation speed [rpm]	Maximal torque [N m]	Gearbox
X	AM8033	6000	15.5	5:1
Y	AM8032	6000	11.7	8:1
Z	AM8023	9000	6.37	10:1
ϕ	AM8043	2500	29.3	/

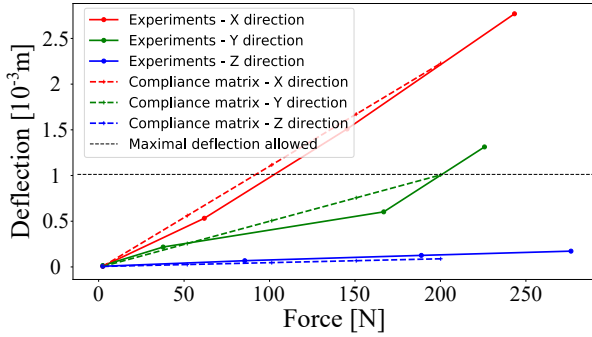


Fig. 4. End-effector deflection of the robot under various external forces in the corresponding directions (solid curves). Dashed curves depict the compliance matrix model derived from experimental results. The horizontal dashed line represents the maximal deflection according to the specifications.

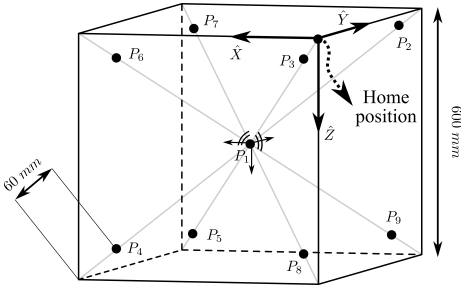


Fig. 5. Specific points used for the experiment within the Cyber-Physical system workspace, inspired by the ISO 9283 standard [22]. These points are located on the medians of the largest cube that can be inserted in the robot workspace, at a distance of $0.1L$ (where L is the cube side length, i.e. 0.6 m here) of the cube vertices.

Figure 4 also provides the predicted displacement according to this interpolated compliance matrix C .

IV. EXPERIMENT 2 : KINEMATIC CHARACTERIZATION

A. Methods

In order to validate the robot range of motion, maximum velocity, and maximum acceleration, the robot is tasked to follow a particular path within its cubic workspace, as represented in Figure 5. The robot starts from position P_8 and goes to P_4 , P_5 , P_7 and then back to P_8 . The path is then composed of four different submovements : the first three along each of the X, Y and Z directions and the fourth one being a diagonal trajectory coupling all directions together. These submovements are separated by 0.3 s standstill phases. Trapezoidal velocity trajectories are followed for each of the four submovements, i.e. a constant acceleration phase, followed by a constant velocity phase and ended with a constant deceleration phase [21]. The constant velocity is set as 1.2 m s^{-1} and the deceleration and acceleration phases are equal in absolute value. The trajectory is performed 34 times, such that the acceleration varies between 1 and 17.5 m s^{-2} by steps of 0.5 m s^{-2} in order to highlight different dynamic effects occurring during these trials. Within a single path, the four submovements have the same trajectory acceleration except when they reach their limit, which are 7 , 17.5 , 15.5 and 12.5 m s^{-2} for the submovements in the X, Y, Z directions and the diagonal respectively.

B. Results

The results of the second experiment are illustrated in Figure 6. Positions, velocities, and accelerations for each axis are depicted, validating the expected robot kinematics. The X linear system shows the largest oscillations, especially in the acceleration signal, which is expected knowing that this linear system has been designed for a lower maximal acceleration than the one applied. Figure 7 shows the impact of the acceleration on the trajectory error for each axis and for the diagonal movement. This error first grows linearly as a function of the acceleration, until an acceleration saturation is reached where the error grows exponentially. This acceleration saturation occurs at around 5 , 13.5 and 15.5 m s^{-2} in the X, Y and Z directions respectively, which is more than twice the desired maximal accelerations from the specifications.

V. EXPERIMENT 3 : VIBRATION CHARACTERIZATION

A. Methods

The objective of the third experiment is to characterize the robot end-effector natural frequency of vibration over its workspace to avoid resonance phenomenon, which would negatively affect control performance. In order to measure the robot end-effector vibrations, using an accelerometer is one of the most efficient methods, according to [23]. Here, we used an Inertial Measurement Unit (IMU) from x-io technologies (Bristol, UK). This sensor is precisely aligned with the Cartesian movement directions and records the accelerations in these directions with a sample rate of 400 Hz , a measurement range of $\pm 16\text{ g}$ and a resolution of 16 bits (i.e. $2,44e^{-4}\text{ g}$). This sensor size is $56 \times 39 \times 18\text{ mm}$ and weighs 56 g . It is attached to the robot end-effector as rigidly as possible — through the use of duct tape and zip ties — in order to minimize its movements during operation.

To generate vibrations at the robot end-effector, the robot performs an impulse movement at one of the nine predefined points within the robot workspace displayed in Figure 5,

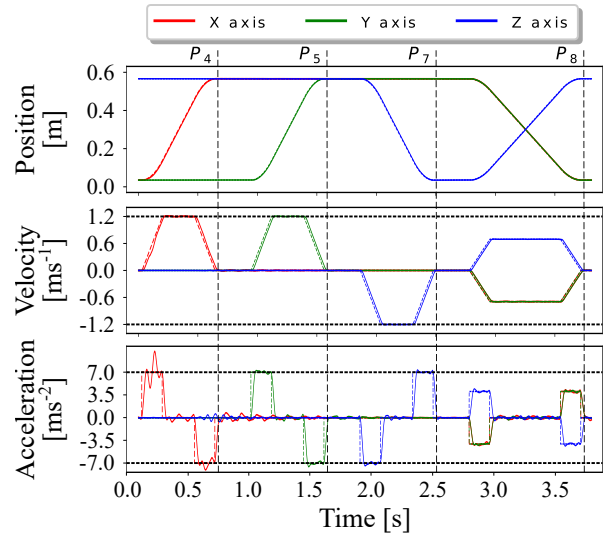


Fig. 6. Trajectory tracking for the path P_8 - P_4 - P_5 - P_7 - P_8 composed of four trapezoidal velocity profiles with a 1.2 m s^{-1} constant velocity and 7 m s^{-2} constant acceleration. The horizontal dashed line represents the maximal acceleration or velocity from the specifications.

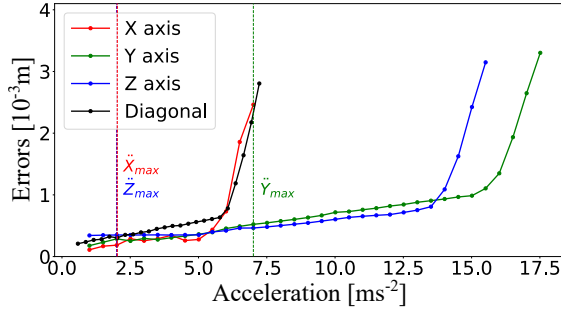


Fig. 7. Maximal trajectory tracking errors for trapezoidal velocity profiles with 1200 mm s^{-1} constant velocity and varying constant acceleration/deceleration. The guiding systems show an acceleration saturation at around 5 , 13.5 and 15.5 ms^{-2} in the X, Y and Z directions respectively. The diagonal movement saturates together with the earliest axis, i.e. with the X direction.

chosen in accordance with the guidelines outlined in the ISO 9283 standard [22]. This movement is a predefined trajectory executed by the robot while recording the resulting vibrations from the IMU. The advantage of this excitation method compared to using a physical impactor [24, 25] is that the amplitude, contingent upon the excitation intensity, remains comparable between each excitations. Additionally, this excitation approach eliminates the need for an external mechanical device [26, 27].

The predefined trajectory applied to the robot is implemented as a trapezoidal velocity profile, with an acceleration/deceleration of 7 m s^{-2} and a travel distance of 50 mm within the workspace. The maximal velocity reached is around 0.592 m s^{-1} , i.e. about 59% of the maximal velocity of the robot in the X and Z directions and 29.6% of the maximal velocity of the robot in the Y direction. This impulse is repeated in each Cartesian direction. Five sets of excitation and resulting acceleration signals are acquired, and the results (i.e. frequencies and amplitudes) are averaged. In the context of this experiment, the influence of other directions is considered negligible. To characterize the vibration signals, their Fast Fourier Transform (FFT) is computed and the frequency with the power peak is highlighted. Moreover, two parameters are computed. First, the maximal amplitude, which is the maximal acceleration obtained during the oscillating period. Then, the damping ratio ξ , which is obtained as $\xi = \frac{\ln(2)}{2\pi m_{50\%}}$ where $m_{50\%}$ is the number of cycles required to reach half of the acceleration. Depending on ξ , the system is said to be undamped ($\xi = 0\%$), underdamped ($\xi < 100\%$), critically damped ($\xi = 100\%$) or overdamped ($\xi > 100\%$) [27, 28].

B. Results

The Waterfall diagram in Figure 8 displays the frequencies derived from the Fast Fourier Transform (FFT) of oscillations generated by three distinct stimulation directions at each of the nine defined points (as specified in Figure 5). The natural frequency of the end-effector is intricately linked to both the stimulation direction and the position of the end-effector within the workspace. For each direction of stimulation, the maximal and minimal natural frequencies across the entire workspace are reported. The range of natural frequencies

spans from 13.7 Hz to 19 Hz , 8.8 Hz to 9.1 Hz and 14.1 Hz to 18.2 Hz for X, Y and Z stimulation directions, respectively. The range of damping ratio and maximal amplitude over the nine different tested points are reported in Table III.

TABLE III
RANGE OF THE DAMPING RATIO AND OSCILLATION MAXIMAL ACCELERATION FOR THE DIFFERENT STIMULATION DIRECTIONS AND OVER THE WORKSPACE.

Direction	Damping ratio [%]	Maximal acceleration [mm s^{-2}]
X	0.8 - 2.32	212 - 1082
Y	0.79 - 1.63	421 - 955
Z	0.88 - 2.55	172 - 558

VI. DISCUSSION AND CONCLUSION

In this study, a robotic Cyber-Physical System (CPS) tailored for flow-device interaction experiments has been designed and preliminarily validated.

Experiment 1 reveals a deviation from specified requirements, notably an exceeding end-effector deflection in the X direction. It is imperative to recognize that these specifications are grounded upon theoretical assumptions for yet-to-be-constructed mechanical devices, subjected to fluid forces. Addressing this discrepancy involves tailored design adjustments to mitigate estimated forces and curtail deflection. The compliance matrix exhibits dominance in its diagonal elements, except for the Z direction because of its higher stiffness. The compliance matrix also reveals that some deformations are poorly captured by a first-order model, likely due to the robot non-linear geometry. This is highlighted by non-symmetry of the non-diagonal elements involved in the Z direction. A limitation of our first experiment is that we tested loading forces in one direction only, for each of the Cartesian axes. Higher-order effects would have been easier to visualize if forces in both directions were performed. This is left for future work, together with the elaboration of a more complex deflexion model that could be used in the robot controller for deflexion compensation and/or for data post-processing.

The second experiment serves as a validation of both kinematic and dynamic specifications. The robot adeptly traverses the entire workspace while adhering to specified

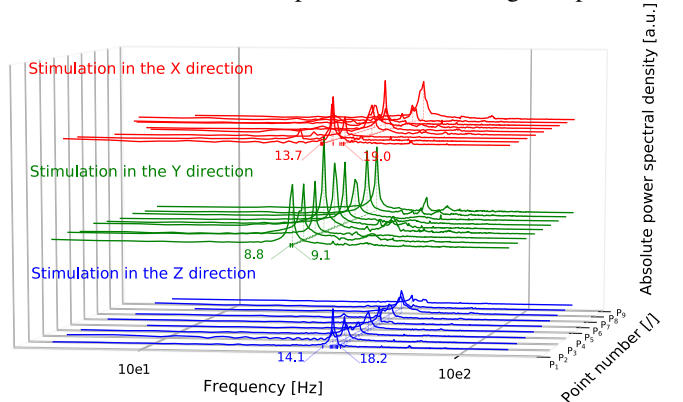


Fig. 8. Waterfall frequency diagram for the stimulations along the three Cartesian directions and for each of the nine points P_i along the workspace. For each stimulation direction, the range of frequencies corresponding to the power peak along the nine points are highlighted.

velocities and accelerations. However, excessive robot acceleration induces trajectory tracking errors due to motor torque saturation. Importantly, this phenomenon occurs for accelerations higher than the maximal ones established in the specifications.

The final experiment, scrutinizing the natural frequency of the robot vibration, shows a damping ratio relatively constant along the stimulation directions. Moreover, it highlights higher vibrations in the X and Y directions, as compared to the Z direction. This is consistent with the earlier observation reporting a higher stiffness in the Z direction. In general, the amplitude of motion due to an external excitation increases as the frequency of that excitation comes closer to the vibration natural frequency. This effect is mitigated if the damping ratio is high enough (typically larger than 50%), capturing that energy at the natural frequency gets quickly dissipated. This is however not the case in our design. In sum, the combination of the damping factors and the frequency analysis underscores the need to avoid the 8 – 19Hz range in future experiments.

Future work will consist in achieving closed-loop manipulations of objects interacting with a fluid environment, through admittance or impedance control [29]. We will likely opt for admittance control, taking force as input and velocity as output, like a majority of other CPS.

In summary, the comprehensive assessment of the newly designed robotic CPS in diverse experimental scenarios yields insights being crucial for refining mechanical design, optimizing control strategies, and informing future experimental considerations. These findings contribute to enhancing the system robustness and performance within the realm of flow-device interaction experiments.

REFERENCES

- [1] M. J. Elzinga, "Flight dynamics in *Drosophila* through a dynamically-scaled robotic approach."
- [2] R. C. Nelson, "Dynamic Behavior of an Aircraft Encountering Aircraft Wake Turbulence," *Journal of Aircraft*, vol. 13, no. 9, pp. 704–708, Sept. 1976. DOI:10/b2fpvb
- [3] U. Schumann and R. Sharman, "Aircraft Wake-Vortex Encounter Analysis for Upper Levels," *Journal of Aircraft*, vol. 52, no. 4, pp. 1277–1285, July 2015. DOI:10/f7tjbx
- [4] C. Bernier, M. Gazzola, P. Chatelain, and R. Ronsse, "Numerical Simulations and Development of Drafting Strategies for Robotic Swimmers at Low Reynolds Number," in *2018 7th IEEE International Conference on Biomedical Robotics and Biomechanics (Biorob)*, 2018.
- [5] Y. Matar, "Etude expérimentale de la nage anguilliforme: application à un robot biomimétique," Ph.D. dissertation, Ecole des Mines de Nantes, 2013.
- [6] Li Wen, Tianmiao Wang, Guanhao Wu, and Jinlan Li, "A novel method based on a force-feedback technique for the hydrodynamic investigation of kinematic effects on robotic fish," in *2011 IEEE International Conference on Robotics and Automation*. Shanghai, China: IEEE, May 2011, pp. 203–208.
- [7] L. Wen, T. Wang, G. Wu, and J. Liang, "Quantitative Thrust Efficiency of a Self-Propulsive Robotic Fish: Experimental Method and Hydrodynamic Investigation," *IEEE/ASME Transactions on Mechatronics*, vol. 18, no. 3, pp. 1027–1038, June 2013. DOI:10/f44dcs
- [8] V. Colognesi, "Modeling and simulation of bird flapping flight : control, wakes and formation," Ph.D. dissertation, UCL - Université Catholique de Louvain, 2022.
- [9] S. J. Portugal, T. Y. Hubel, J. Fritz, S. Heese, D. Trobe, B. Voelkl, S. Hailes, A. M. Wilson, and J. R. Usherwood, "Upwash exploitation and downwash avoidance by flap phasing in ibis formation flight," *Nature*, vol. 505, no. 7483, pp. 399–402, Jan. 2014. DOI:10/f5m87w
- [10] R. S. Sutton and A. G. Barto, *Reinforcement Learning, Second Edition: An Introduction*. MIT Press, Nov. 2018.
- [11] T. D. Buchanan and W. A. Crosby, "Captive Trajectory System Test Planning Information for AEDC Supersonic Wind Tunnel (A) and Hypersonic Wind Tunnels (B) and (C)," Defense Technical Information Center, Fort Belvoir, VA, Tech. Rep., Dec. 1983.
- [12] A. W. Mackowski and C. H. Williamson, "Developing a cyber-physical fluid dynamics facility for fluid–structure interaction studies," *Journal of Fluids and Structures*, vol. 27, no. 5-6, pp. 748–757, July 2011. DOI:10/csmvxx
- [13] F. Hover, S. Miller, and M. Triantafyllou, "VORTEX-INDUCED VIBRATION OF MARINE CABLES: EXPERIMENTS USING FORCE FEEDBACK," *Journal of Fluids and Structures*, vol. 11, no. 3, pp. 307–326, Apr. 1997. DOI:10/ckpc9g
- [14] Y. Goodwin, *Wind Tunnel Study of Rotating/Flapping Wing Flow*, June 2022.
- [15] C. P. Fagley, J. Seidel, and T. E. McLaughlin, "Experimental Investigation of the Aeroelastic Behavior a NACA0018 Cyber-Physical FlexibleWing," in *33rd AIAA Applied Aerodynamics Conference*. Dallas, TX: American Institute of Aeronautics and Astronautics, June 2015.
- [16] R. Waghela, M. Bryant, and F. Wu, "Control design in cyber-physical fluid–structure interaction experiments," *Journal of Fluids and Structures*, vol. 82, pp. 86–100, Oct. 2018. DOI:10.1016/j.jfluidstructs.2018.06.018
- [17] K. Onoue, A. Song, B. Strom, and K. S. Breuer, "Large amplitude flow-induced oscillations and energy harvesting using a cyber-physical pitching plate," *Journal of Fluids and Structures*, vol. 55, pp. 262–275, May 2015. DOI:10.1016/j.jfluidstructs.2015.03.004
- [18] K. Onoue and K. S. Breuer, "Vortex formation and shedding from a cyber-physical pitching plate," *Journal of Fluid Mechanics*, vol. 793, pp. 229–247, Apr. 2016. DOI:10.1017/jfm.2016.134
- [19] H. Sun, E. Soo Kim, M. P. Bernitsas, and M. M. Bernitsas, "Virtual Spring–Damping System for Flow-Induced Motion Experiments," *Journal of Offshore Mechanics and Arctic Engineering*, vol. 137, no. 6, p. 061801, Dec. 2015. DOI:10.1115/1.4031327
- [20] B. A. GmbH and C. Kg, "Dokumentation AX5000 Tuning - Guide."
- [21] B. Siciliano and O. Khatib, Eds., *Springer Handbook of Robotics*. Berlin: Springer, 2008.
- [22] *ISO 9283, Manipulating Industrial Robots - Performance Criteria and Related Test Methods*, Second edition ed., Switzerland, Apr. 1998.
- [23] D. Goyal and B. S. Pabla, "The Vibration Monitoring Methods and Signal Processing Techniques for Structural Health Monitoring: A Review," *Archives of Computational Methods in Engineering*, vol. 23, no. 4, pp. 585–594, Dec. 2016. DOI:10.1007/s11831-015-9145-0
- [24] P. Glogowski, M. Rieger, J. B. Sun, and B. Kuhlenkötter, "Natural Frequency Analysis in the Workspace of a Six-Axis Industrial Robot Using Design of Experiments," *Advanced Materials Research*, vol. 1140, pp. 345–352, Aug. 2016. DOI:10/gtfz4
- [25] C. Bisu, M. Cherif, A. Gerard, and J. Y. K'nevez, "Dynamic Behavior Analysis for a Six Axis Industrial Machining Robot," *Advanced Materials Research*, vol. 423, pp. 65–76, Dec. 2011. DOI:10/fx8bj5
- [26] L. Sun, F. Liang, and L. Fang, "Chatter Vibration Analysis of A Novel Industrial Robot for Robotic Boring Process," in *2018 IEEE International Conference on Intelligence and Safety for Robotics (ISR)*, Aug. 2018, pp. 56–60.
- [27] D. Hao, W. Wang, Z. Liu, and C. Yun, "Experimental study of stability prediction for high-speed robotic milling of aluminum," *Journal of Vibration and Control*, vol. 26, no. 7-8, pp. 387–398, Apr. 2020. DOI:10/gtfzgx
- [28] C. Saldarriaga, N. Chakraborty, and I. Kao, "Damping Selection for Cartesian Impedance Control With Dynamic Response Modulation," *IEEE Transactions on Robotics*, vol. 38, no. 3, pp. 1915–1924, June 2022. DOI:10/gtfzgr
- [29] R. Waghela and M. Bryant, "Control Design for High-Fidelity Cyber-Physical Systems With Applications to Experimental Fluid-Structure Interaction Studies," in *Volume 2: Modeling, Simulation and Control of Adaptive Systems; Integrated System Design and Implementation; Structural Health Monitoring*. Snowbird, Utah, USA: American Society of Mechanical Engineers, Sept. 2017.